



Inverse-designed ultra-compact star-crossings based on PhC-like subwavelength structures for optical intercross connect

LULUZI LU, MINMING ZHANG,* FEIYA ZHOU, WEIJIE CHANG, JIANG TANG, DONGYU LI, XINSHU REN, ZEPENG PAN, MENG FAN CHENG, AND DEMING LIU

School of Optical and Electrical Information, Huazhong University of Science and Technology, Wuhan, 430074, China

*mmz@mail.hust.edu.cn

Abstract: With the development of highly densified photonic integrated circuits, the optical cross nodes number exhibits dramatically increasing. Not only efficient but also ultra-compact waveguide crossings are required to materialize the full potential of silicon photonics for on-chip optical intercross connect. In this work, we proposed several inverse-designed 4×4 , 5×5 and 6×6 star-crossings based on the photonic-crystal-like (PhC-like) subwavelength structures, which have ultra-high port density of about $7.1 \mu\text{m}^2/\text{port}$, $5.83 \mu\text{m}^2/\text{port}$ and $7.3 \mu\text{m}^2/\text{port}$ respectively. Moreover, the star-crossings are practically fabricated and experimentally characterized. The average measured insertion losses (ILs) are less than 0.75, 0.9 dB and 1.5 dB, while the crosstalks are sub-22.5 dB, -20 dB and -18 dB for other output ports over 60 nm bandwidth centered at 1550 nm wavelength.

© 2017 Optical Society of America

OCIS codes: (160.3918) Metamaterials; (130.3120) Integrated optics devices; (130.5296) Photonic crystal waveguides.

References and links

1. W. Bogaerts, P. Dumon, D. V. Thourhout, and R. Baets, "Low-loss, low-cross-talk crossings for silicon-on-insulator nanophotonic waveguides," *Opt. Lett.* **32**(19), 2801–2803 (2007).
2. T. Fukazawa, T. Hirano, F. Ohno, and T. Baba, "Low loss intersection of Si photonic wire waveguides," *Jpn. J. Appl. Phys.* **43**(2), 646–647 (2004).
3. W. Bogaerts, P. Dumon, D. Van Thourhout, and R. Baets, "Low-loss, low-cross-talk crossings for silicon-on-insulator nanophotonic waveguides," *Opt. Lett.* **32**(19), 2801–2803 (2007).
4. H. Chen and A. W. Poon, "Low-loss multimode-interference-based crossings for silicon wire waveguides," *IEEE Photonics Technol. Lett.* **18**(21), 2260–2262 (2006).
5. Y. Li, C. Xu, C. Zeng, W. Wang, J. Yang, H. Yu, and X. Jiang, "Hybrid plasmonic waveguide crossing based on the multimode interference effect," *Opt. Commun.* **335**, 86–89 (2015).
6. A. M. Jones, C. T. DeRose, A. L. Lentine, D. C. Trotter, A. L. Starbuck, and R. A. Norwood, "Ultra-low crosstalk, CMOS compatible waveguide crossings for densely integrated photonic interconnection networks," *Opt. Express* **21**(10), 12002–12013 (2013).
7. Y. Zhang, A. Hosseini, X. Xu, D. Kwong, and R. T. Chen, "Ultralow-loss silicon waveguide crossing using Bloch modes in index-engineered cascaded multimode-interference couplers," *Opt. Lett.* **38**(18), 3608–3611 (2013).
8. P. J. Bock, P. Cheben, J. H. Schmid, J. Lapointe, A. Del  ge, D.-X. Xu, S. Janz, A. Densmore, and T. J. Hall, "Subwavelength grating crossings for silicon wire waveguides," *Opt. Express* **18**(15), 16146–16155 (2010).
9. P. Sanchis, P. Villalba, F. Cuesta, A. H  kansson, A. Griol, J. V. Gal  n, A. Brimont, and J. Mart  , "Highly efficient crossing structure for silicon-on-insulator waveguides," *Opt. Lett.* **34**(18), 2760–2762 (2009).
10. Y. Zhang, S. Yang, A. E.-J. Lim, G.-Q. Lo, C. Galland, T. Baehr-Jones, and M. Hochberg, "A CMOS-compatible, low-loss, and low-crosstalk silicon waveguide crossing," *IEEE Photonics Technol. Lett.* **25**(5), 422–425 (2013).
11. Y. Ma, Y. Zhang, S. Yang, A. Novack, R. Ding, A. E. Lim, G. Q. Lo, T. Baehr-Jones, and M. Hochberg, "Ultralow loss single layer submicron silicon waveguide crossing for SOI optical interconnect," *Opt. Express* **21**(24), 29374–29382 (2013).
12. T. Niwa, H. Hasegawa, and K. Sato, "A 270 x 270 Optical Cross-connect Switch Utilizing Wavelength Routing with Cascaded AWGs," in *Optical Fiber Communication Conf./Nat. Fiber Optic Engineers Conf. 2013*, OSA Technical Digest (online) (Optical Society of America, 2013), paper OTh1A.3.

13. A. Y. Piggott, J. Lu, K. G. Lagoudakis, J. Petykiewicz, T. M. Babinec, and J. Vučković, "Inverse design and demonstration of a compact and broadband on-chip wavelength demultiplexer," *Nat. Photonics* **9**(6), 374–377 (2015).
14. B. Shen, P. Wang, R. Polson, and R. Menon, "Q"An integrated-nanophotonics polarization beamsplitter with $2.4 \times 2.4 \mu\text{m}^2$ footprint," *Nat. Photonics* **9**(6), 378–382 (2015).
15. A. Y. Piggott, J. Lu, T. M. Babinec, K. G. Lagoudakis, J. Petykiewicz, and J. Vučković, "Inverse design and implementation of a wavelength demultiplexing grating coupler," *Sci. Rep.* **4**(1), 7210 (2015).
16. L. Lu, D. Liu, F. Zhou, D. Li, M. Cheng, L. Deng, S. Fu, J. Xia, and M. Zhang, "Inverse-designed single-step-etched colorless 3 dB couplers based on RIE-lag-insensitive PhC-like subwavelength structures," *Opt. Lett.* **41**(21), 5051–5054 (2016).
17. Lumerical FDTD solutions, <https://www.lumerical.com>.
18. W. Ding, D. Tang, Y. Liu, L. Chen, and X. Sun, "Compact and low crosstalk waveguide crossing using impedance matched metamaterial," *Appl. Phys. Lett.* **96**(11), 111114 (2010).
19. G. Ren, T. G. Nguyen, and A. Mitchell, "Gaussian Beams on a Silicon-on-Insulator Chip Using Integrated Optical Lenses," *IEEE Photonics Technol. Lett.* **26**(14), 1438–1441 (2014).
20. J. Zou, Y. Yu, and X. Zhang, "Single step etched two dimensional grating coupler based on the SOI platform," *Opt. Express* **23**(25), 32490–32495 (2015).
21. Y. Ding, H. Ou, and C. Peucheret, "Ultrahigh-efficiency apodized grating coupler using fully etched photonic crystals," *Opt. Lett.* **38**(15), 2732–2734 (2013).

1. Introduction

As the complexity of photonics integrated circuits (PICs) increase and more devices are supposed to be placed on a single chip, the number of the cross nodes of the waveguides in the optical paths would increase quadratically with the number of the channels. Different approaches for optimizing the performance of the 2×2 waveguide crossing have been reported, including using adiabatic mode expansion [1–3], multimode interference (MMI) [4, 5], multilevel waveguide bridge [6], low loss Bloch modes [7, 8] and geometry optimization [9–11] etc. Very attractive device performance like 0.02 dB insertion loss and -40 dB crosstalk has been achieved in the last decade. However, when there are large scales of optical channels to intercross, e.g. the number of channels to intercross can reach 9 in an optical cross connect (OXC) system with cascade cyclic array waveguide gratings (AWGs) [12], the footprint of the components utilizing conventional 2×2 crossings would be extremely large. Figure 1(a) shows a typical waveguide layout in an optical intercross connect. Six 2×2 crossings and at least two bending waveguides are needed for 4×4 intercross connect. The area for crossing may climb to about $256 \mu\text{m}^2$ in order to minimize the crosstalk and the bending loss. The "port density" (device area divided by port number) of the intercross connect is about $64 \mu\text{m}^2/\text{port}$. A star-crossing shown in Fig. 1(b), with only one lumped node, could remarkably improve the port density and expand the capacity of the optical circuits. However, the IL and crosstalk of a simple star-crossing would be rather high, due to the strong reflection and diffraction effects at the cross region.

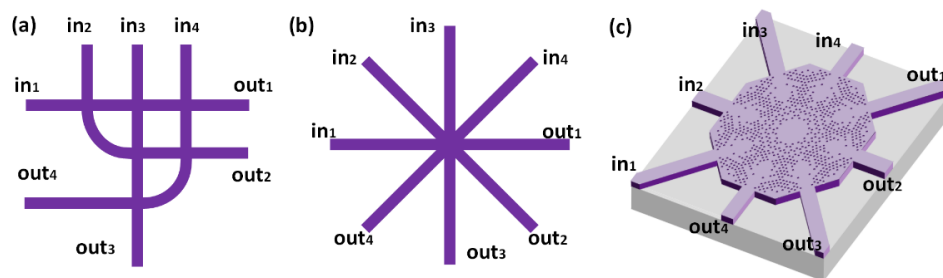


Fig. 1. (a-b) The illustrations of a 4×4 intercross employing 6 conventional 2×2 crossings and only 1 single-node star-crossing respectively. (c) A top view of the proposed 4×4 star-crossing.

On the other hand, recently, the inverse-designed free-form nanophotonic structures, which enable one to manipulate the flow of light tremendously, have shown great potential in

designing ultra-compact integrated photonic devices, such as wavelength demultiplexer [13], polarization beamsplitter [14], wavelength demultiplexing grating coupler [15], and optical coupler [16] etc. Among those free-form metamaterial structures which are too precise for practical fabrication, the PhC-like subwavelength structure illustrated in [16] has been proved to be insensitive to the fabrication errors, such as reactive ion etching (RIE) lag effect.

Thus, in this work, we utilize the PhC-like metamaterial structure to inversely design several star-crossings, to realize 4×4 , 5×5 and 6×6 intercross connects. The lengths of the star-crossings are only $5.33 \mu\text{m}$, $6.63 \mu\text{m}$ and $6.61 \mu\text{m}$ respectively. By adding a coupling region with the PhC-like structure and optimizing the circular holes' combination, one can dramatically suppress the reflection and diffraction in the coupling region and reduce the IL and crosstalk of the star-crossings. Figure 1(c) shows an illustration of the 4×4 star-crossing, which has a port density of about $7.1 \mu\text{m}^2/\text{port}$ and is almost an order of magnitude smaller than the one constituted of conventional 2×2 crossings in Fig. 1(a). The simulated average ILs of are about 0.5 dB, 0.75 dB and 1.1 dB over 80 nm centered 1550 nm wavelength for 4×4 , 5×5 and 6×6 star-crossings respectively. Moreover, these star-crossings are experimentally fabricated and the measured ILs are less than 0.75 ± 0.2 dB, 0.9 ± 0.2 dB and 1.5 ± 0.2 dB over 60 nm bandwidth.

2. Design of the proposed star-crossings

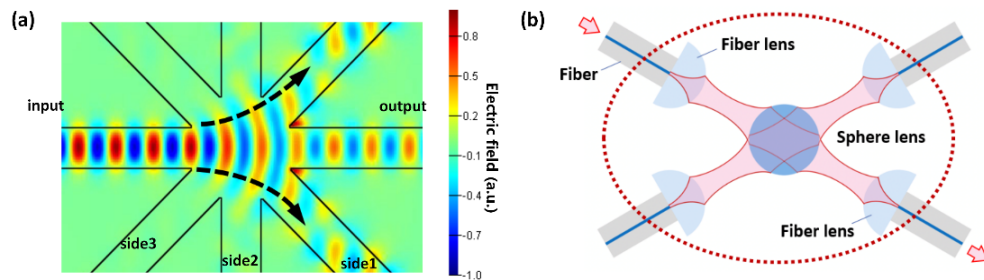


Fig. 2. (a) The electric field distribution of the device in Fig. 1(b). (b) The illustration of a 3-lens system.

The simulated electric field distribution [17] of the simple star-crossing in Fig. 1(b) is shown in Fig. 2(a). It can be seen that the tiny light beam of the guided modes of the input waveguide will diverge significantly due to the effect of diffraction when it transmits through the central crossing region. The larger the divergence angle is, the less (more) power would be coupled into the output (adjacent) waveguide, which is the main cause of a high IL (crosstalk) [18]. In free space, as shown in Fig. 2(b), one can improve the performance of an optical fiber based star-crossing using three-lens systems: the light beam from the input port is firstly expanded by a fiber lens, then collimated by a sphere lens, and finally focused and coupled into the output port by another fiber lens. If we design such lens appropriately, the divergence or diffraction of all light beams can be restrained effectively. And as a consequence, the IL and crosstalk would decrease greatly. Similarly, one may design high performance planar star-crossings using planar lenses based three-lens system [19]. Here, we add a coupling region based on the PhC-like metamaterial structure to realize such three-lens system using inverse design methods. Furthermore, such structure could also be employed to eliminate the Fresnel reflection loss of conventional silicon slab lenses caused by the large refractive index difference between silicon and air.

The proposed star-crossings are fabricated on a silicon-on-insulator (SOI) platform with 220 nm-thick top silicon layer. The first challenge to design the devices is to find a proper way to place those circular pixels in the coupling region. A simple circular symmetric combination may lead the pixels to be too sparse whereas too tight at the edge. Thus, the index control for different areas in the coupling region are imbalance and not highly efficient.

So, we adopt a 1/8, 1/10 or 1/12 circular symmetric combination to our proposed star-crossings.

To begin with, the outline of the coupling regions of our proposed star-crossings are set to be regular polygon and each triangle district is axisymmetric. Figure 3(a) shows the detailed holes' combination rules: the holes are arranged in lines, which are parallel to the symmetric axis, and the periods are alternate between x_1 and x_2 ; the distance between the lines are y . We tune x_1 , x_2 and y to ensure the distances between the holes, i.e. the 3 kinds of distances (α , β , and γ), marked by double-arrow lines in Fig. 3(a), are no less than 125nm, to prevent the silicon wall between the holes being etched through. For an $M \times M$ star-crossing, the geometries of α , β , and γ are:

$$\alpha = 2x_1 \cdot \sin\left(\frac{\pi}{2M}\right) \quad (1),$$

$$\beta = \sqrt{\left[x_2 \cdot \cot\left(\frac{\pi}{2M}\right) - x_1\right]^2 + y^2} \quad (2),$$

$$\gamma = \sqrt{\left[x_1 + x_2 - y \cdot \cot\left(\frac{\pi}{2M}\right)\right]^2 + y^2} \quad (3).$$

The values of x_1 , x_2 and y are all preferred to be as small as possible so that there would be more pixels in the coupling region, making the control of index, i.e. the light flow, more effective. Besides, in order to prevent the quite thin silicon walls between such holes and the device boarder from being etched through, an additional silicon wall, the light gray area in Fig. 3(b), outside the pixelated area is added to ensure that the wall thickness is no less than 60 nm.

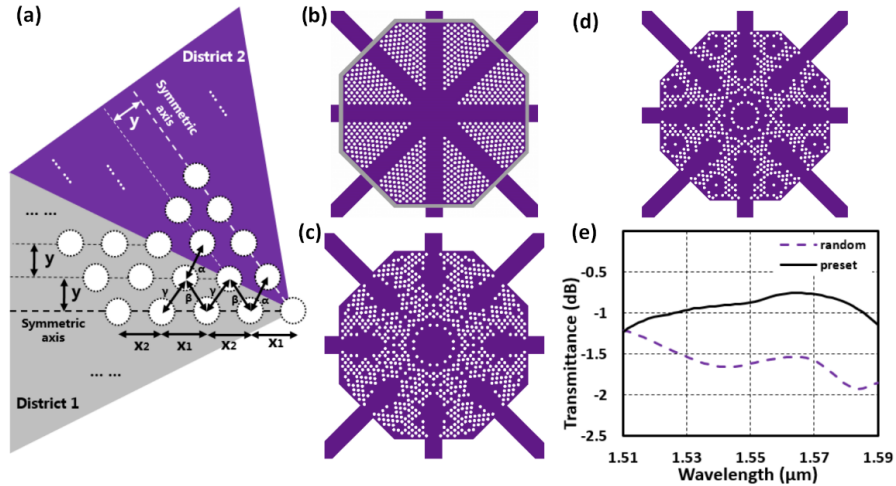


Fig. 3. (a) The illustration of the holes' combination rules; (b) are the preset initial pattern of the simulation for the 4×4 star-crossing; (c-d) are the optimum patterns for preset and random initials; (e) shows the transmittances of devices in (c) and (d) with solid and dashed lines respectively.

Here, we take the 4×4 star-crossing as an example for detailed description. x_1 and x_2 are set to be equal to 160 nm. And y is set to be 99.5 nm. The grey area is set to be 25 nm thick. The length of the coupling region is set to be $5.33 \mu\text{m}$ with 33 periods. The port density of the device is about $7.1 \mu\text{m}^2/\text{port}$. The holes have a radius of 45 nm, and their depth is chosen to be 140 nm at first, (considering the lag effect, the depth of the holes is not the ideal 220nm in a normal one-step etching process [20]). The width of the waveguides is 500nm.

As shown in Fig. 3(b), we manually set an initial pattern, motivated by the imitation of a normal star-crossing: the 5 lines of holes closest to the center symmetric axis in every district are set to be '1', i.e. the holes are not etched; other lines of holes are set to be '0', i.e. the holes are etched.

The figure-of-merit (FOM) of the device for inverse design is defined as

$$FOM = 1 - \frac{1}{N} \cdot \sum (1-t) \quad (4),$$

where t is the optical power transmittance of the direct output port. N is the number of wavelengths and five wavelengths over 80 nm range are taken into consideration in our simulations. Thus, the second item on the right side of Eq. (1) stands for the average transmittance. For an ideal crossing, the $FOM = 1$. The items which depict reflection and crosstalks are not considered in the FOM, since they are linearly related to the transmittance.

The nonlinear direct-binary-search (DBS) optimization algorithm is used to figure out a local optimum hole combination with a similar process described in [8, 10]. Generally, we toggle the state of the two axisymmetric pixels in each district and evaluate the FOM. If the FOM get improved, then the new state is kept and the next 16 pixels are toggled. When the FOM exhibits no improvement after one iteration, the optimization ends. The 3D FDTD simulation [17] is used to calculate the optical distributions.

Figure 3(c) shows an optimized pattern (after 8 iterations) for the preset initial in Fig. 3(b) and the simulated IL of the device is shown in Fig. 3(e). Actually, some totally random initial patterns are tried first, but some of them may converge to relatively degraded local optimums: Fig. 3(d) shows an optimized pattern for a random initial. Its IL, as shown in Fig. 3(e), is 0.7 dB in average more than that of the device in Fig. 3(c).

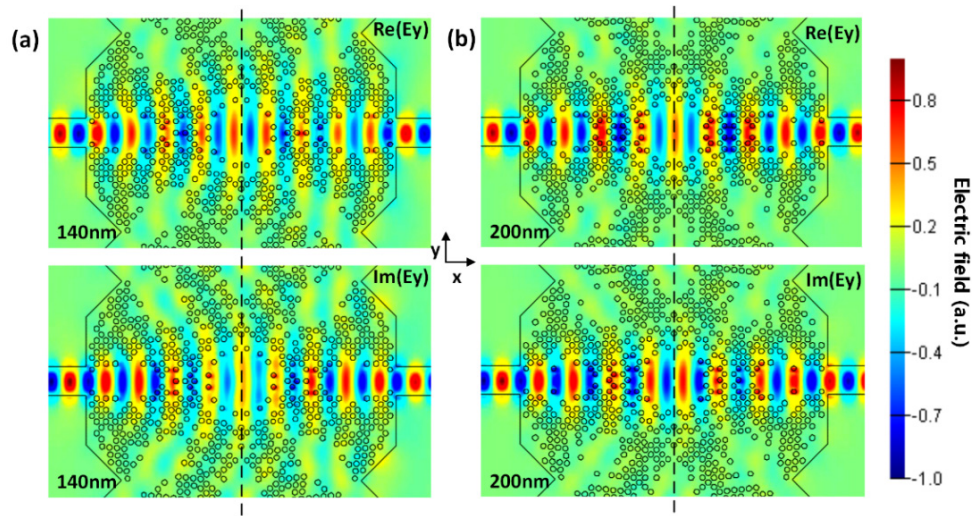


Fig. 4. (a) and (b) are the real/imaginary parts of the simulated electric field distributions of the optimized device with etching depth of 140 nm and 200 nm at 1550 nm wavelength respectively.

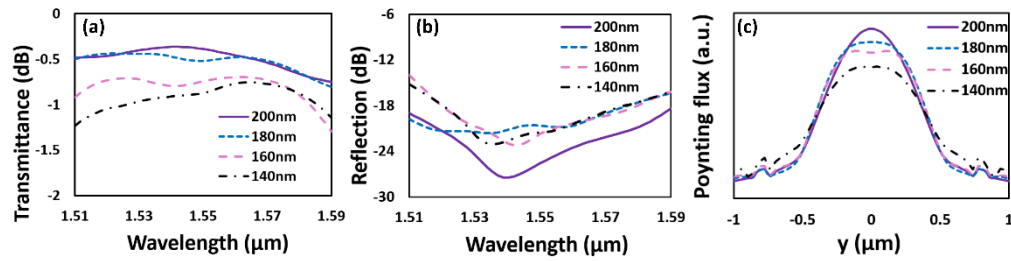


Fig. 5. (a)-(b) The simulated transmittances and reflections of the optimized devices with different etching depths of 140 nm (dot dash), 160 nm (long dash), 180 nm (short dash) and 200 nm (solid) respectively. (c) depicts the normalized Poynting flux along the center symmetric axis of the optimized devices at 1550 nm wavelength respectively.

However, the average IL of the device is still up to 0.85 dB as shown in Fig. 3(c). Figure 4(a) shows the real and imaginary parts of the simulated electric field distribution of the device in Fig. 3(c) at 1550 nm wavelength respectively. According to the flow of light, the proposed star-crossing works in a similar way as a three-lens system: the center pattern of the device forms a subwavelength planar circular lens, and the patterns between the central part and the in-/out- put waveguide work as subwavelength planar beam expanders. But, for an ideal three-lens system, the electrical field on the two sides of the center symmetric axis (shown with dashed line in Fig. 4) should be complex conjugate. It is obvious that the electric field distribution in Fig. 3 (a) is quite far from that goal.

In order to refine our design, we increase the etching depth for further index control of the coupling region. Figure 5(a) shows the simulated transmittances of the optimized devices with three other different etching depths of 160 nm, 180 nm and 200 nm in comparison to the one of 140 nm etched device. And the reflection losses are shown in Fig. 5(b) respectively. The normalized Poynting flux at 1550 nm wavelength along the center symmetric axis can be seen in Fig. 5(c). Since the center part of the coupling region works as a planar circular lens, the optical power beyond the edge of the lens would be dissipated. Thus, the 200 nm-etched device, which has the smallest mode field diameter, has the lowest IL, around 0.4 dB at 1550 nm wavelength. Figure 4(b) shows the electric field distribution of the 200 nm-etched device, which present an almost axi-symmetric complex conjugate field, confirming the way how the star-crossings work. Figure 6(a) shows the optimized pattern (after 7 iterations) of the device with 200 nm etching depth and its crosstalk can be observed in Fig. 6(b), less than -21 dB over 80 nm bandwidth.

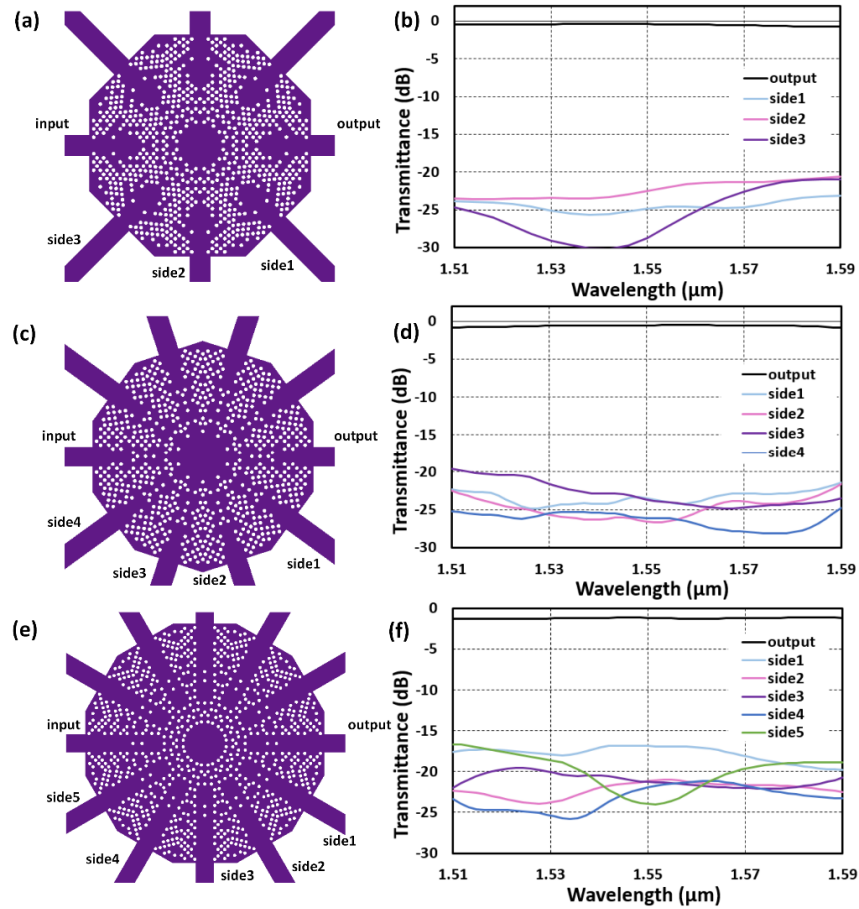


Fig. 6. (a), (b) and (e) are the top views of the optimized devices with 8, 10 and 12 ports. (b), (d) and (f) are the transmittances of the straight output ports and the side output ports of the left devices respectively.

With the same optimization process, the optimum patterns of the 5×5 and 6×6 star-crossings, as shown in Figs. 6(c) and 6(e), can be obtained after 9 and 7 iterations respectively. For the 5×5 star-crossing, x_1 and x_2 are equal to 200 nm. y is set to be 97.5 nm. And the coupling region lengths is $5.41 \mu\text{m}$ including the 5 nm-thick grey wall. For the 6×6 one, we employ $x_1 = 250 \text{ nm}$, $x_2 = 183.7 \text{ nm}$ and $y = 92 \text{ nm}$. The coupling region lengths is $6.6 \mu\text{m}$ including the 50 nm-thick grey wall. Both of the two devices has a hole etching depth of 200 nm. And their port densities are 5.83 and $7.3 \mu\text{m}^2/\text{port}$ respectively. Their ILs of each output port are shown in Fig. 6(d) and 6(f) respectively. The average IL and crosstalks for the 5×5 star-crossing are $0.75 \text{ dB/sub} -20 \text{ dB}$ over 80 nm bandwidth, $1.1 \text{ dB/sub} -16 \text{ dB}$ for the 6×6 one.

3. Experiment results

The star-crossings are fabricated using an electron-beam lithography (EBL) system (Vistec EBPG 5000 Plus) to pattern a 330 nm ZEP-520A electron-beam resist layer spun on the samples, and an inductively coupled plasma (ICP) etcher (Plasmalab System100) to transfer the mask to the silicon device layer. For a usual single-step etching process, the etching time is controlled to etch the strip waveguides just fully (220nm), which is called the “full-etching time”. However, due to the RIE lag effect, the exact etch depth of circular holes with radius of 45 nm would be only around 140 nm [16]. We designed test chips with lines of holes with

different radii on SOI wafers, did the etching processes with different etching time, and measured their etching depths. At last, the 1.6 times of the full-etching time is employed to fabricate our proposed star-crossings designed with 200 nm etching depth.

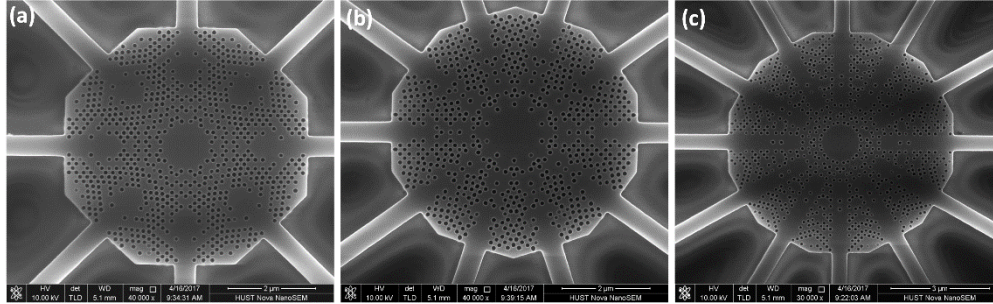


Fig. 7. (a)-(c) The SEM pictures of the fabricated 4×4 , 5×5 and 6×6 star-crossings respectively.

The scanning electron microscope (SEM) picture of the star-crossings are shown in Figs. 7(a)-7(c) respectively. A broadband amplifier spontaneous emission (ASE) light source was vertically coupled into the input port by an improved chirped 1D grating coupler which can adapt to over-etching process [21]. The same grating couplers were used at the output ports and an optical spectrum analyzer (Yokogawa AQ6370C-20) was employed to measure the light coupled out. We also designed and fabricated reference components consisting of two coupling gratings connected by a waveguide. The structure of the gratings and the total lengths of the waveguide of the star-crossing and the reference components were identical. By subtracting the measured ILs of the reference component from those of the star-crossing, one can obtain the exact ILs of the SW structure. However, it's always difficult to measure a sub 1 dB IL precisely since the measuring error will have a serious influence on the accuracy. An efficient way to extract the insertion loss accurately is utilizing test structures with different numbers of cascaded devices, and for our case we take numbers to be 1 and 5.

The measured and simulated transmittances profiles of the straight output port of each single device are shown in Figs. 8(a), 8(c) and 8(e) respectively. The curve with the legend of "5 crossings/5" means the average transmittance of a single crossing (divide the measured total transmittance of five cascade crossings by 5). For the cascaded devices, every two adjacent crossings are connected with a waveguide with the same length of around $55 \mu\text{m}$. So, there may be four equivalent Fabry-Perot (F-P) cavities and each one consists of two adjacent ports with limit return loss and a waveguide bridging the ports. As a result, regular valleys would appear in the transmittance profile of the cascaded devices due to a limit free spectral range (around $6 \times \text{nm}$) of such F-P cavities. Figures 8(b), 8(d) and 8(f) depict the crosstalks of the side output ports of the devices respectively. Generally, the ILs of the 4×4 , 5×5 and 6×6 star-crossings are $0.75 \pm 0.2 \text{ dB}$, $0.9 \pm 0.2 \text{ dB}$ and $1.5 \pm 0.2 \text{ dB}$, and their crosstalks are about -22.5 dB , -20 dB and -18 dB respectively over about 60 nm bandwidth (1520nm-1580nm).

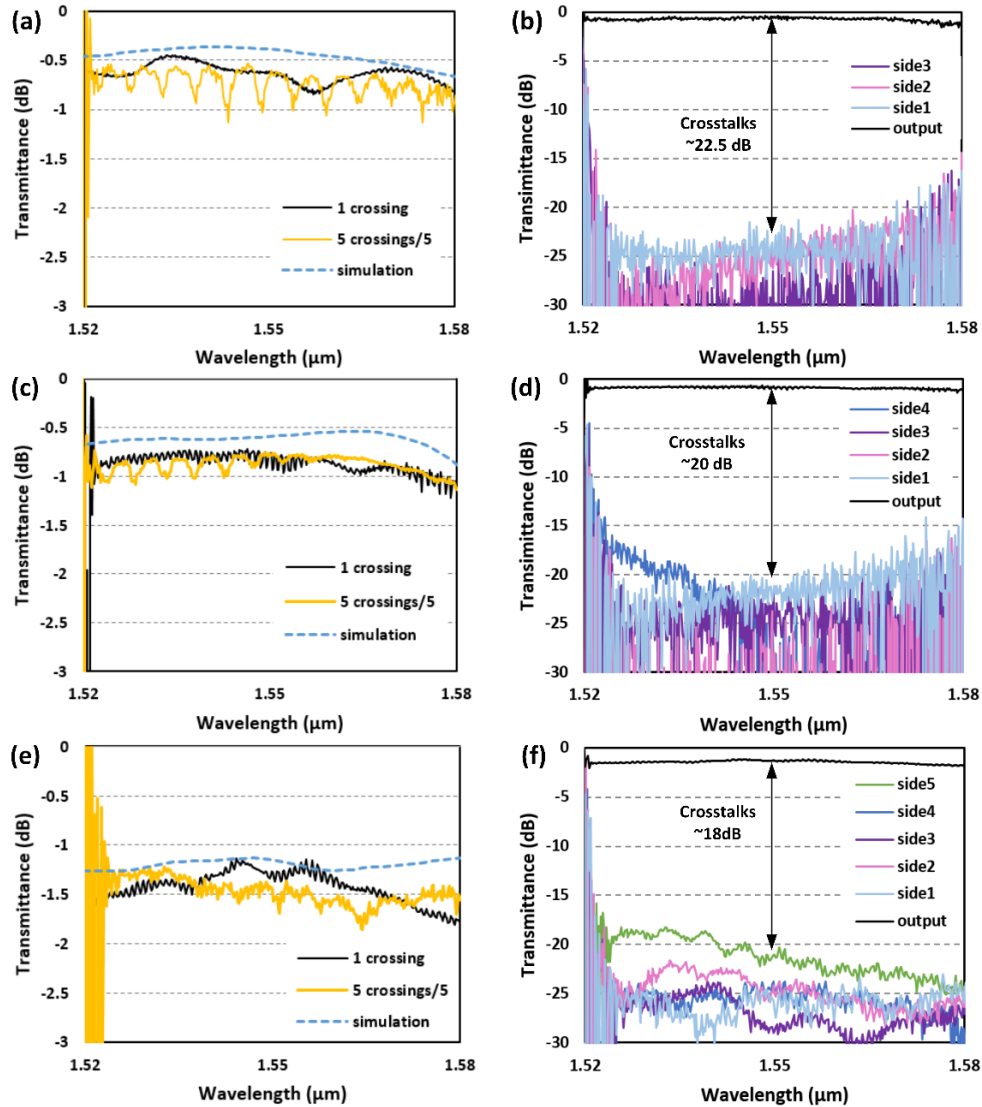


Fig. 8. (a), (c) and (e) are the measured transmittances of a single device (in black) and the average transmittance of a single crossing (in orange) for the 4×4 , 5×5 and 6×6 star-crossings respectively. (b), (d) and (f) show the crosstalks of the side output ports of each device respectively.

Finally, to further investigate the fabrication accuracy acquisition of the proposed structure, star-crossings with the same pattern but different hole radii from 39 to 51 nm with a step of 2.5 nm were designed and fabricated using the same etching process. The measured average IL increased about 0.6 dB and 0.9 dB for ± 2.5 nm and ± 5 nm radii changes, respectively, compared with the device with a hole radius of 45 nm, which means that the PhC-like subwavelength structure-based star-crossings were robust to fabrication errors of hole radius.

4. Conclusion

Ultra-compact 4×4 , 5×5 and 6×6 star-crossings for optical intercross connect, with ultra-high port density of about $7.1 \mu\text{m}^2/\text{port}$, $5.83 \mu\text{m}^2/\text{port}$ and $7.3 \mu\text{m}^2/\text{port}$ respectively, are designed based on the PhC-like subwavelength structure using nonlinear DBS algorithm. The

star-crossings with subwavelength patterns work as a three-lens system, showing great potential in further improvement of port density. The designed star-crossings are practically fabricated and characterized. The measured average ILs of the devices are 0.75 ± 0.2 dB, 0.9 ± 0.2 dB and 1.5 ± 0.2 dB over 60 nm bandwidth, respectively. Finally, we also experimentally demonstrated that the crossings are robust enough to sustain ± 5 nm fabrication errors of the hole radius at the cost of 0.9 dB IL increase. Compared with pioneering work, the port density of the devices is quite attractive and offers the capability of developing integrated photonic components to be more densified on SOI platforms, which may help to promote practical applications of nanostructure components greatly.

Funding

This work is partially supported by the National High Technology Research and Development Program of China (863 Program, Grand No. 2015AA015504) and the Major Project of Science and Technology Innovation Program of Hubei Province of China (Grand No. 2014AAA006) and National Natural Science Foundation of China (Grand No. 61635004 and 61107051)

Acknowledgments

The authors thank Xiangjie Zhao, He Zhang and Liangqiu Zhu engineers in the Center of Micro-Fabrication and Characterization (CMFC) of Wuhan National Laboratory for Optoelectronics (WNLO) for the support in EBL and ICP etching processes.